

Capillary rise of a liquid into a deformable porous material

J. I. Siddique,^{a)} D. M. Anderson,^{b)} and Andrei Bondarev^{c)}

Department of Mathematical Sciences, George Mason University, Fairfax, Virginia 22030, USA

(Received 25 September 2008; accepted 12 December 2008; published online 27 January 2009)

We examine the effects of capillarity and gravity in a model of one-dimensional imbibition of an incompressible liquid into a deformable porous material. We focus primarily on a capillary rise problem but also discuss a capillary/gravitational drainage configuration in which capillary and gravity forces act in the same direction. Models in both cases can be formulated as nonlinear free-boundary problems. In the capillary rise problem, we identify time-dependent solutions numerically and compare them in the long time limit to analytically obtain equilibrium or steady state solutions. A basic feature of the capillary rise model is that, after an early time regime governed by zero gravity dynamics, the liquid rises to a finite, equilibrium height and the porous material deforms into an equilibrium configuration. We explore the details of these solutions and their dependence on system parameters such as the capillary pressure and the solid to liquid density ratio. We quantify both net, or global, deformation of the material and local deformation that may occur even in the case of zero net deformation. In the model for the draining problem, we identify numerical solutions that quantify the effects of gravity, capillarity, and solid to liquid density ratio on the time required for a finite volume of fluid to drain into the deformable porous material. In the Appendix, experiments on capillary rise of water into a deformable sponge are described and the measured capillary rise height and sponge deformation are compared with the theoretical predictions. For early times, the experimental data and theoretical predictions for these interface dynamics are in general agreement. On the other hand, the long time equilibrium predicted theoretically is not observed in our experimental data. © 2009 American Institute of Physics.

[DOI: [10.1063/1.3068194](https://doi.org/10.1063/1.3068194)]

I. INTRODUCTION

In this article we develop a model for capillary rise into a deformable porous material. Capillary rise phenomena occur in both rigid and deformable materials in a wide variety of scientific fields such as oil recovery, inkjet printing, textile engineering, and flows in biological tissues. There is interest in this subject from the point of view of both industrial research and fundamental science. The present work addresses modeling and solutions of this problem that contribute to a better understanding of capillary rise into deformable porous materials.

The pioneering study of Washburn¹ described fluid flow into a rigid porous material. This model was based on the assumption that the porous material was a collection of small cylindrical capillaries, and the flow through these capillaries was Poiseuille flow subject to a pressure difference acting to force the liquid in the capillaries. In the absence of gravity, the volume of the liquid that penetrates into the porous material in a time t is proportional to \sqrt{t} . In contrast, when gravity is present the liquid rises to a finite, equilibrium height. The Washburn model has been widely used to describe capillary rise phenomena in rigid nondeformable porous materials.

Recently, Zhmud *et al.*² studied the dynamics of capillary rise in rigid porous materials. They showed that a num-

ber of models, including the Washburn model, describing dynamics of capillary rise can be obtained as particular limiting cases of a more general equation based on Newtonian dynamics. They also showed that these general equations were in qualitative agreement with their experimental results.

However, other recent experimental investigations have revealed capillary rise behavior in rigid porous materials that departs notably from the Washburn predictions. Delker *et al.*³ performed experiments on capillary rise of water through a packing of glass beads. Their early time data for capillary rise height follow a $t^{1/2}$ power law, but for longer times the advancing front rises beyond the Washburn equilibrium height. Lago and Araujo⁴ also observed similar dynamics in their experiments of capillary rise in an array of packed spheres. Both studies identified a new power law scaling for this longer time regime that was close to $t^{1/4}$.

Davis and Hocking^{5,6} considered a variety of models for liquid spreading and imbibition into a rigid porous base. In their first model⁵ they assumed that the porous material was uniform and isotropic in structure. The flow in the porous substrate was described by Darcy's law. In this model they considered the partially saturated case in which the wetted portion of the substrate was assumed to extend to the bottom of the porous substrate. In their second model⁶ they extended their previous work to include spreading above an initially dry porous substrate. In this model they assumed that there was no cross linking of the capillaries in the substrate which was also the case in the Washburn model. They calculated the penetration shapes as a function of time.

^{a)}Electronic mail: jsiddiqu@gmu.edu.

^{b)}Electronic mail: danders1@gmu.edu.

^{c)}Co-author of Appendix. Electronic mail: abondar1@gmu.edu.

The above discussion outlines briefly some of the classical as well as more recent studies involving flows in rigid porous materials. Here we turn our attention to porous materials which deform when liquid passes through them, e.g., spongelike materials. Deformable porous materials arise in various fields, including geophysics,⁷ soil science,^{8–10} infiltration,^{11–15} snow physics,¹⁶ paper and printing,^{17,18} and medical science.^{19–27} In such cases, the flow through the deformable porous media deforms the material due to the forces associated with flow. The material deformation in turn influences the flow. Models that account for both flow and deformation are required to analyze the dynamics of these materials.

Early models of flows in deformable porous media were developed to study soil consolidation. Biot²⁸ described a problem involving deformable porous media in which Darcy's law, used to describe the fluid flow, was coupled to a linear elasticity model for the solid deformation. He presented the solutions for soil consolidation in one dimension as well as two dimensions under permeable²⁹ and impermeable³⁰ rectangular loads.

Our approach follows more recent work in which the porous material is modeled as a mixture of solid and fluid. In mixture theory each component is treated as a single continuum and every point in space is considered to be occupied by a particle belonging to each component of the mixture at each instant of time. A detailed mixture theory description is presented by several authors.^{31,32}

Barry and Aldis^{25,26} examined a variety of different models of deformable porous media based on mixture theory. These models include cases of flow induced deformation from pressurized cavities in absorbing porous tissues and radial flow through deformable porous shells. In their flow induced deformation model, biological tissues are modeled as nonlinear deformable porous media where the deformation of the tissues in turn alters the flow. In the case of radial flow, a governing system of equations was developed for cylindrical and spherical geometries.

Hou *et al.*²⁴ studied the formulation of boundary conditions between a viscous fluid and a biphasic mixture. They used binary mixture theory to develop a set of boundary conditions based on conservation laws. These conditions were validated by applying them to Poiseuille flow and Couette flow problems.

Barry *et al.*²⁷ revisited the work of Hou *et al.*²⁴ for fluid flow over a thin deformable porous layer. Binary mixture theory was used to obtain the governing system of equations with assumptions that solid deformation was infinitesimal and the predominant displacement was along the axis of the channel. Wang and Parker³³ examined the effect of deformable porous surface layers on the motion of a sphere in a narrow cylindrical tube. They also used binary mixture theory for solid and liquid constituents to model the porous layer on both the surface of the tube and the sphere. They applied lubrication theory in the region between the sphere and the wall in order to study the effects of deformable layers on the motion of the sphere.

Sommer and Mortensen¹¹ considered the forced unidirectional infiltration in an initially dry deformable porous

material. A constant applied pressure drove the fluid flow in the porous material. Agreement between their model and the experimental results was reported.

Preziosi *et al.*¹² studied the infiltration of a liquid into a deformable porous material. In this model, an initially dry and compressed porous material was infiltrated by an incompressible liquid which caused the porous material to deform and relax.

Following this work, Anderson³⁴ presented a model for the imbibition of a liquid droplet on a deformable porous substrate using the deformation model of Preziosi *et al.* For the assumed one-dimensional material deformation, a model for the imbibition of liquid into the porous material and also for the porous material deformation was developed. Anderson's model, which did not include gravitational effects, predicted that during the imbibition of liquid into the deformable porous substrate, swelling, swelling relaxation, and shrinking of the porous material could occur.

The ideas used for modeling deformable spongelike materials also have application to problems involving suspensions and gels. Manley *et al.*³⁵ performed experiments and examined a model for gravitational collapse of colloidal gels. Their model was based on a Darcy's equation similar to the one we use here. Approximations, such as negligible fluid velocity relative to the solid velocity and constant solid volume fraction, lead to a gel height that decays exponentially in time to an equilibrium height determined by a balance of gravitational and elastic forces. Kim *et al.*³⁶ examined a similar problem that addresses gravitational collapse and stabilization of a suspension of attractive colloidal particles. Their mathematical model is very similar to ours but differs in details including boundary conditions as we discuss further in the next section.

Dufresne *et al.*^{37,38} studied related systems involving the flow and fracture in drying nanoparticle suspensions. Here the compaction of the material is driven by evaporation and fluid flow at the drying surface. The dynamics of the compaction front, crack formation in the drying suspension, and long time crack propagation were investigated.

In the present work, we consider capillary rise of a fluid into a deformable porous material. Our model is an analog of the Washburn model¹ of capillary rise into a rigid porous material. The basic governing equations for flow in deformable material follow those of several previous authors.^{11,12,21,25,26,34} Our model follows most closely that of Preziosi *et al.*,¹² Barry and Aldis,^{25,26} and Anderson.³⁴ We are interested in examining gravitational effects; these have been included in previous models,^{12,25,26} but the corresponding solutions have not been addressed. Additionally, with the Washburn model and the experiments of Delker *et al.*³ and Lago and Araujo⁴ in mind, in the Appendix we compare our work with experiments on capillary rise of water into deformable porous sponges.

In Sec. II, we present the one-dimensional capillary rise problem and then nondimensionalize the governing system of equations. In Sec. III, we present equilibrium and time-dependent solutions of the capillary rise problem. In Sec. IV results and discussion of the capillary rise problem are given. In Sec. V we discuss the drainage problem and its solutions.

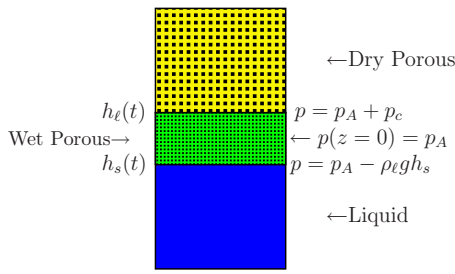


FIG. 1. (Color online) This figure shows the one-dimensional capillary rise configuration.

Section VI contains the conclusions. Finally, the Appendix gives details of experiments on the dynamics of capillary rise of water into deformable porous sponges and makes comparisons with the theory.

II. ONE-DIMENSIONAL MODEL

We consider a one-dimensional deformable spongelike material in contact with a liquid. The upper end of the deformable material is fixed. At time $t=0$, the contact position of the deformable material and liquid is defined by $z=0$. It is assumed that the imbibition of fluid occurs from an infinite bath of fluid whose upper surface at $z=0$ remains open to atmospheric pressure (i.e., $p=p_A$ at $z=0$ for all time). For $t > 0$ the liquid rises into an initially dry porous material due to capillary suction in the pore space of the porous material assuming the capillary pressure $p_c < 0$, which results in deformation of the porous material. The upper interface of the wet porous material region is defined by $z=h_\ell(t)$ and the lower interface formed after the deformation is defined by $z=h_s(t)$ as shown in Fig. 1. We have assumed that the pressure in the fluid bath is hydrostatic. This implies that $p=p_A - \rho_\ell g h_s$ at $z=h_s(t)$. The dry porous material is rigid and has uniform solid fraction ϕ_0 .

As a result of the above assumptions, the only remaining unknowns are those in the wet material and the boundary positions h_s and h_ℓ . The variables of interest in the wet region are the solid fraction ϕ , the vertical velocity component of the liquid phase w_ℓ , the vertical velocity component of solid phase w_s , the liquid pressure p , and the stress in the solid σ where $\sigma = \sigma \mathbf{I}$. The set of equations for the one-dimensional material deformation can be written as

$$\frac{\partial \phi}{\partial t} + \frac{\partial}{\partial z}(\phi w_s) = 0, \quad (1)$$

$$\frac{\partial \phi}{\partial t} - \frac{\partial}{\partial z}[(1-\phi)w_\ell] = 0, \quad (2)$$

$$w_\ell - w_s = -\frac{K(\phi)}{(1-\phi)\mu} \left(\frac{\partial p}{\partial z} + \rho_\ell g \right), \quad (3)$$

$$0 = -\frac{\partial p}{\partial z} + \frac{\partial \sigma}{\partial z} - g[\rho_s \phi + \rho_\ell (1-\phi)], \quad (4)$$

where ρ_s and ρ_ℓ are the true intrinsic densities of solid and liquid, respectively, and are assumed to be constant. The per-

meability $K(\phi)$ and solid stress $\sigma(\phi)$, whose forms we specify below, are functions of the local solid volume fraction, μ is the dynamic viscosity, and g is the gravitational acceleration. Equations (1)–(4) are consistent with those of previous authors.^{12,25,26} More specifically, Eqs. (1) and (2) are the mass balance equations for solid and liquid phases, respectively, where the assumption of constant density has been taken into account. Equations (3) and (4) are reduced from general solid and liquid momentum balances [e.g., see Eqs. (3) and (4) of Preziosi *et al.*]. In particular, our Eq. (4) represents a combined momentum balance of the fluid-solid mixture. Note that we have assumed that inertial terms and viscous stresses are negligible and that stress tensors and frictional forces between phases take forms standard in mixture theory [e.g., see Eqs. (16) and (17) of Barry and Aldis²⁶]. In this case the only velocity terms in the momentum balances appear in the relative velocity of the modified Darcy equation (3). Our new contribution is to examine in detail solutions of these equations and boundary conditions we specify below in order to assess gravitational effects on the flow and deformation.

Equations (1)–(4) can be reduced to a single partial differential equation for the solid fraction ϕ , as in Ref. 34. Subtracting Eq. (2) from Eq. (1) and integrating once gives

$$\phi w_s + (1-\phi)w_\ell = c(t), \quad (5)$$

where $c(t)$ is a function determined by the boundary conditions. Equations (3) and (5) allow us to write formulas for liquid and solid velocities as follows:

$$w_\ell = c(t) - \frac{\phi K(\phi)}{(1-\phi)\mu} \left(\frac{\partial p}{\partial z} + \rho_\ell g \right), \quad (6)$$

$$w_s = c(t) + \frac{K(\phi)}{\mu} \left(\frac{\partial p}{\partial z} + \rho_\ell g \right). \quad (7)$$

Since the stress is a function of the solid volume fraction $\sigma = \sigma(\phi)$, Eq. (4) can be written as follows:

$$\frac{\partial p}{\partial z} = \sigma'(\phi) \frac{\partial \phi}{\partial z} - g[\rho_s \phi + \rho_\ell (1-\phi)]. \quad (8)$$

After combining Eqs. (1), (7), and (8), we get the equation for ϕ ,

$$\frac{\partial \phi}{\partial t} + c(t) \frac{\partial \phi}{\partial z} = -\frac{\partial}{\partial z} \left[\frac{\phi K(\phi)}{\mu} \left\{ \sigma'(\phi) \frac{\partial \phi}{\partial z} - g(\rho_s - \rho_\ell) \phi \right\} \right], \quad (9)$$

on $h_s(t) < z < h_\ell(t)$. When gravity is absent, Eq. (9) is equivalent to Eq. (44) of Preziosi *et al.*¹² and Eq. (20) of Anderson.³⁴ The same partial differential equation (PDE) for ϕ can be seen in the work of Kim *et al.*³⁶ by interpreting our $K(\phi)$ as their $\kappa(\phi)$, our μ as their η , our $\sigma'(\phi)$ as their $-K(\phi)/\phi$, and our $c(t)=0$. The case $c(t)=0$ follows if the solid and liquid velocities are zero at the bottom boundary, as in Ref. 36. While their final equation is the same as ours, we note that their stress balance [their Eq. (5)] and continuity equation [their Eq. (6)] involve $\partial p/\partial z$ rather than $\partial p/\partial z + \rho_\ell g$.

The boundary conditions applied at the liquid–wet material interface $z=h_s(t)$ are

$$w_s(h_s^+, t) = \frac{\partial h_s}{\partial t}, \quad (10)$$

$$p(h_s^+, t) = p_A - \rho_\ell g h_s(t), \quad (11)$$

$$\sigma(h_s^+, t) = 0, \quad (12)$$

where p_A is atmospheric pressure. Equations (10)–(12) are the kinematic condition, hydrostatic pressure assumption in the liquid bath, and zero stress condition, respectively.

The boundary conditions applied at the wet material–dry material interface $z=h_\ell(t)$ are

$$w_\ell(h_\ell^-, t) = \frac{\partial h_\ell}{\partial t}, \quad (13)$$

$$p(h_\ell^-, t) = p_A + p_c, \quad (14)$$

where p_c is a constant capillary pressure. Here Eqs. (13) and (14) are the kinematic and capillary pressure conditions, respectively.

Following Preziosi *et al.* and Anderson, an expression for the $c(t)$ can be written as

$$c(t) = -\frac{(1-\phi_0)}{\phi_0} \left[\frac{\phi K(\phi)}{\mu(1-\phi)} \left(\sigma'(\phi) \frac{\partial \phi}{\partial z} - g(\rho_s - \rho_\ell) \phi \right) \right] \Bigg|_{h_\ell^-}. \quad (15)$$

The combination of Eqs. (6)–(8) with Eqs. (10) and (13) yields equations for interface positions,

$$\frac{\partial h_s}{\partial t} = c(t) + \frac{K(\phi)}{\mu} \left(\sigma'(\phi) \frac{\partial \phi}{\partial z} - g(\rho_s - \rho_\ell) \phi \right) \Bigg|_{h_s^+}, \quad (16)$$

$$\frac{\partial h_\ell}{\partial t} = c(t) - \frac{\phi K(\phi)}{\mu(1-\phi)} \left(\sigma'(\phi) \frac{\partial \phi}{\partial z} - g(\rho_s - \rho_\ell) \phi \right) \Bigg|_{h_\ell^-}. \quad (17)$$

To summarize, we need to solve Eqs. (8) and (9) subject to Eqs. (11), (12), and (14) where the free surface positions are determined by Eqs. (16) and (17) along with appropriate initial conditions. Note that Eq. (9) is coupled to Eq. (8) and the pressure via the boundary conditions.

A. Nondimensionalized system of equations

Before solving the time-dependent problem we introduce the following dimensionless quantities for space, time, interface positions, and pressure:

$$\bar{z} = \frac{z - h_s(t)}{h_\ell(t) - h_s(t)}, \quad \bar{t} = \frac{t}{T}, \quad \bar{h}_s = \frac{h_s}{L}, \quad \bar{h}_\ell = \frac{h_\ell}{L}, \quad \bar{p} = \frac{p}{m}, \quad (18)$$

where $L = m/\rho_\ell g$ and $T = L^2 \mu / m K_0$. Here K_0 and m are the permeability and stress scales defined below. These choices of dimensionless variables allow us to transform the moving boundary problem to a fixed domain problem.

Our choices for permeability $K(\phi)$ and stress $\sigma(\phi)$, which are consistent with physically realistic trends, are $K(\phi) = K_0/\phi$, where $K_0 > 0$ and $\sigma(\phi) = m(\phi_r - \phi)$.³⁴ We take $m > 0$ so that $\sigma'(\phi) = -m < 0$. The assumed form of the stress function is suitable for our one-dimensional deformation model; in higher dimensions, this would need to be generalized to account for effects such as shear deformation. Note that σ is positive for $\phi < \phi_r$ (i.e., expansion relative to the relaxed state) and negative for $\phi > \phi_r$ (i.e., compression relative to the relaxed state). According to this choice, when solid fraction is at a constant relaxed value ϕ_r , the stress function is zero.

Introducing these choices and dimensionless variables, the PDE for ϕ can be written as

$$\begin{aligned} \frac{\partial \phi}{\partial \bar{t}} + \left[\frac{(\bar{z}-1) \frac{d\bar{h}_s}{d\bar{t}}}{(\bar{h}_\ell - \bar{h}_s) \frac{d\bar{t}}{d\bar{t}}} - \frac{\bar{z}}{(\bar{h}_\ell - \bar{h}_s) \frac{d\bar{t}}{d\bar{t}}} \frac{d\bar{h}_\ell}{d\bar{t}} \right] \frac{\partial \phi}{\partial \bar{z}} + \frac{\bar{c}(\bar{t})}{(\bar{h}_\ell - \bar{h}_s)} \frac{\partial \phi}{\partial \bar{z}} \\ = \frac{1}{(\bar{h}_\ell - \bar{h}_s)^2} \frac{\partial^2 \phi}{\partial \bar{z}^2} + \frac{\rho}{(\bar{h}_\ell - \bar{h}_s)} \frac{\partial \phi}{\partial \bar{z}}, \end{aligned} \quad (19)$$

where $\rho = (\rho_s/\rho_\ell - 1)$. Boundary conditions for solid volume fraction can be derived from the zero stress and stress equilibrium conditions as follows:

$$\phi = \phi_r \quad \text{at } \bar{z} = 0, \quad (20)$$

$$\phi = \phi_\ell^* - (\bar{h}_\ell - \bar{h}_s) \int_0^1 (\rho \phi + 1) d\bar{z} - \bar{h}_s \quad \text{at } \bar{z} = 1, \quad (21)$$

where $\phi_\ell^* = \phi_r - p_c/m$. The boundary condition (21) is obtained by integrating Eq. (8) and applying the pressure boundary conditions (11) and (14). Note that in the absence of gravity Eq. (21) reduces to $\phi = \phi_\ell^*$. The function $\bar{c}(\bar{t})$ is given by

$$\bar{c}(\bar{t}) = \frac{1-\phi_0}{\phi_0} \left[\frac{1}{(1-\phi)(\bar{h}_\ell - \bar{h}_s)} \frac{\partial \phi}{\partial \bar{z}} + \frac{\rho \phi}{(1-\phi)} \right] \Bigg|_{\bar{z}=1}, \quad (22)$$

and dimensionless interface positions satisfy the ordinary differential equations (ODEs)

$$\frac{d\bar{h}_s}{d\bar{t}} = \bar{c}(\bar{t}) - \left[\frac{1}{\phi(\bar{h}_\ell - \bar{h}_s)} \frac{\partial \phi}{\partial \bar{z}} + \rho \right] \Bigg|_{\bar{z}=0}, \quad (23)$$

$$\frac{d\bar{h}_\ell}{d\bar{t}} = \bar{c}(\bar{t}) + \left[\frac{1}{(1-\phi)(\bar{h}_\ell - \bar{h}_s)} \frac{\partial \phi}{\partial \bar{z}} + \frac{\rho \phi}{(1-\phi)} \right] \Bigg|_{\bar{z}=1}. \quad (24)$$

The initial conditions for the interface positions are

$$\bar{h}_\ell(\bar{t}=0) = 0, \quad \bar{h}_s(\bar{t}=0) = 0. \quad (25)$$

III. CAPILLARY RISE SOLUTIONS

The time-dependent free-boundary problem (19)–(25) can be solved numerically. First, however, we will identify the equilibrium state solution which will be compared with the time-dependent solution later in Sec. IV.

A. Steady state solution

The steady state solution for solid volume fraction and pressure can be written as follows:

$$\phi(\bar{z}) = \phi_r e^{\rho(\bar{h}_s^\infty - \bar{h}_\ell^\infty)\bar{z}} \quad (26)$$

and

$$\bar{p}(\bar{z}) = \phi_r - \phi_\ell^* + (\bar{h}_\ell^\infty - \bar{h}_s^\infty)(1 - \bar{z}) + \bar{p}_A \quad (27)$$

where \bar{h}_s^∞ and \bar{h}_ℓ^∞ are the equilibrium heights of solid and liquid, respectively, to be determined. Here \bar{p}_A is the dimensionless atmospheric pressure. This pressure corresponds to hydrostatic pressure and quantity $\phi_r - \phi_\ell^*$ can be interpreted as a dimensionless capillary pressure.

To find the steady state solid interface position \bar{h}_s^∞ , we use a global mass conservation argument which can be stated as follows. The mass of the solid before liquid is imbibed into the material is equal to the mass of the solid after liquid is imbibed into the material. In dimensionless form, this is

$$\phi_0 \bar{h}_\ell^\infty = (\bar{h}_\ell^\infty - \bar{h}_s^\infty) \int_0^1 \phi(\bar{z}) d\bar{z}. \quad (28)$$

The solution of Eq. (28) after using Eq. (26) yields a steady state solid interface position,

$$\bar{h}_s^\infty = \frac{1}{\rho} \ln \left(1 - \rho \bar{h}_\ell^\infty \frac{\phi_0}{\phi_r} \right) + \bar{h}_\ell^\infty. \quad (29)$$

Also the steady state liquid interface position can be written as

$$\bar{h}_\ell^\infty = \phi_\ell^* - \phi_r. \quad (30)$$

Note that in dimensional form $h_\ell^\infty = -p_c / \rho_\ell g$, which is the same as that for capillary rise in a rigid porous material given the same capillary pressure p_c . Using Eqs. (26) and (29) we can define

$$\phi_\ell^\infty = \phi_r - \rho(\phi_\ell^* - \phi_r)\phi_0, \quad (31)$$

where ϕ_ℓ^∞ is the solid volume fraction at the wet material–dry material interface evaluated in the limit $t \rightarrow \infty$. Further discussion of these solutions will be given in Sec. IV. In the following section we will solve the time-dependent capillary rise problem.

B. Time-dependent solution

The coefficients of Eqs. (19), (23), and (24) are singular at time $t=0$. However, in the asymptotic limit $t \rightarrow 0$ these equations and the boundary condition (21) reduce to the zero gravity case. In this case, Eq. (19) with the associated boundary conditions can be solved using the similarity variable η

$= z/2\sqrt{Dt}$, where $D=L^2/T=K_0m/\mu$ has units of length squared per unit time (see Ref. 34 for details). Here the interface positions can be expressed as

$$\bar{h}_s(\bar{t}) = 2\lambda_s \sqrt{\bar{t}}, \quad \bar{h}_\ell(\bar{t}) = 2\lambda_\ell \sqrt{\bar{t}}. \quad (32)$$

The zero gravity solution, denoted by ϕ_s , can be written in terms of the error function as follows:

$$\phi_s = \frac{\text{erf}(\lambda_s - B) - \text{erf}(\eta - B)}{\text{erf}(\lambda_s - B) - \text{erf}(\lambda_\ell - B)} (\phi_\ell^* - \phi_r) + \phi_r, \quad (33)$$

where

$$B = (1 - \phi_0)\lambda_\ell \quad (34)$$

and

$$\lambda_s = \frac{(\phi_\ell^* - \phi_r)}{\sqrt{\pi}[\text{erf}(\lambda_s - B) - \text{erf}(\lambda_\ell - B)]} \left\{ \frac{1}{\phi_r} \exp[-(\lambda_s - B)^2] - \frac{(1 - \phi_0)}{\phi_0(1 - \phi_\ell^*)} \exp[-(\lambda_\ell - B)^2] \right\}, \quad (35)$$

$$\lambda_\ell = - \frac{(\phi_\ell^* - \phi_r) \exp[-(\lambda_\ell - B)^2]}{\phi_0(1 - \phi_\ell^*) \sqrt{\pi}[\text{erf}(\lambda_s - B) - \text{erf}(\lambda_\ell - B)]}. \quad (36)$$

This is the solution given by Anderson,³⁴ Eqs. (46)–(49). We avoid the singularity at $\bar{t}=0$ [when $\bar{h}_s(\bar{t})=\bar{h}_\ell(\bar{t})=0$] numerically when solving Eqs. (19)–(24) by using this similarity solution as an initial condition at time $\bar{t}=\bar{t}_I > 0$. Specifically, the initial condition for ϕ can be derived from the similarity solution $\phi(\bar{z}, \bar{t}_I) = \phi_s(\eta)$, where \bar{t}_I is chosen to be sufficiently small so that the solution is independent of any further reduction in \bar{t}_I . Noting that

$$\eta = \lambda_s + \bar{z}(\lambda_\ell - \lambda_s), \quad (37)$$

the initial condition for ϕ in dimensionless form becomes

$$\phi(\bar{z}, \bar{t} = \bar{t}_I) = \phi_s[\lambda_s + \bar{z}(\lambda_\ell - \lambda_s)]. \quad (38)$$

The initial conditions for \bar{h}_s and \bar{h}_ℓ are

$$\bar{h}_s(\bar{t}_I) = 2\lambda_s \sqrt{\bar{t}_I}, \quad \bar{h}_\ell(\bar{t}_I) = 2\lambda_\ell \sqrt{\bar{t}_I}. \quad (39)$$

The above system of equations (19)–(24) is solved numerically subject to the initial conditions (39) and also by using the similarity solution (38) as an initial condition for ϕ . To compute the numerical solution, we use a method of lines approach with a second order accurate finite difference scheme in space. This converts the PDE to a system of ODEs. These ODEs along with Eqs. (23) and (24) are solved numerically using MATLAB's ode23s solver.

IV. CAPILLARY RISE RESULTS AND DISCUSSION

Figure 2 shows the evolution of interface positions $\bar{h}_s(t)$ ($g=0, g \neq 0$ cases) and $\bar{h}_\ell(t)$ ($g=0, g \neq 0$ cases). In the absence of gravity, $\bar{h}_s(t)$ evolves downward and $\bar{h}_\ell(t)$ evolves upward following a square root in time trend. This is the similarity solution of Anderson.³⁴ For the nonzero gravity case, initially both curves follow the similarity solution but ultimately reach steady state values \bar{h}_s^∞ and \bar{h}_ℓ^∞ . In the Appen-

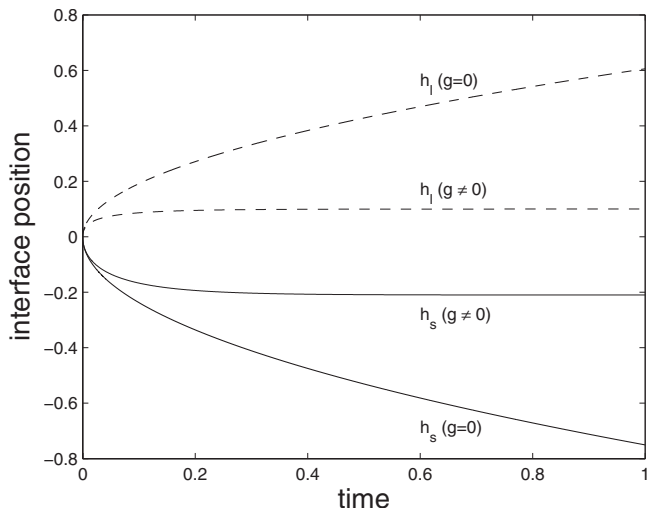


FIG. 2. This figure shows the evolution of the interface positions h_s and h_ℓ for $g=0$ and $g \neq 0$. In this plot we have used $\phi_\ell^*=0.2$, $\phi_r=0.1$, and $\phi_0=0.33$ and for the nonzero gravity case $\rho=0.1$.

dix we compare predictions for these interface positions to the experimental data obtained for the capillary rise of water into deformable sponges for the same configuration examined in the model.

The steady state values for $\bar{h}_s^\infty, \bar{h}_\ell^\infty$ that can be observed in Fig. 2 depend on various parameters. In the next several figures we explore this dependence. We first note that the dimensionless \bar{h}_ℓ^∞ is independent of ρ [see Eq. (30)]. However, it is important to point out that the length scale L and the dimensional h_ℓ^∞ do depend on ρ_ℓ . Therefore, we interpret ρ as a dimensionless quantity measuring solid density.

In Fig. 3, the ratio of \bar{h}_s^∞ and \bar{h}_ℓ^∞ is plotted as a function of ρ . The solid curve represents the analytical solution of \bar{h}_s^∞ and \bar{h}_ℓ^∞ for ρ values ranging from -0.5 to 1 . Four numerically computed values of $h_\ell(t)$ and $h_s(t)$ for sufficiently large

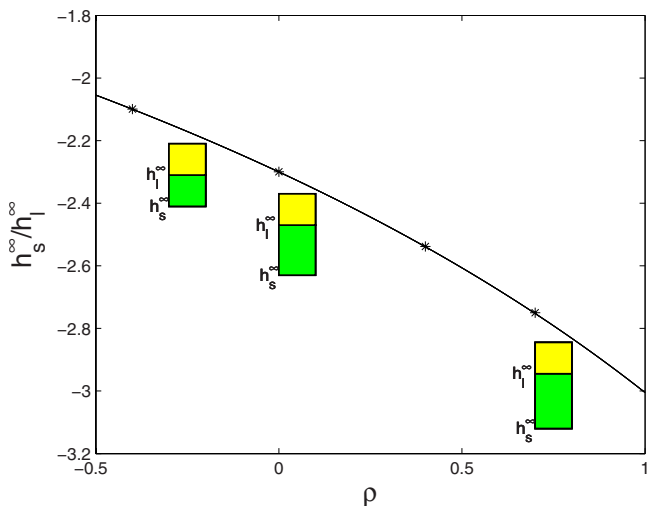


FIG. 3. (Color online) This plot shows the ratio of $\bar{h}_s^\infty/\bar{h}_\ell^\infty$ vs ρ given by Eq. (29). The solid line is analytical solution and “*” is the full numerical solution at large times for different ρ values for fixed values of $\phi_r=0.10$, $\phi_0=0.33$, and $\phi_\ell^*=0.20$.

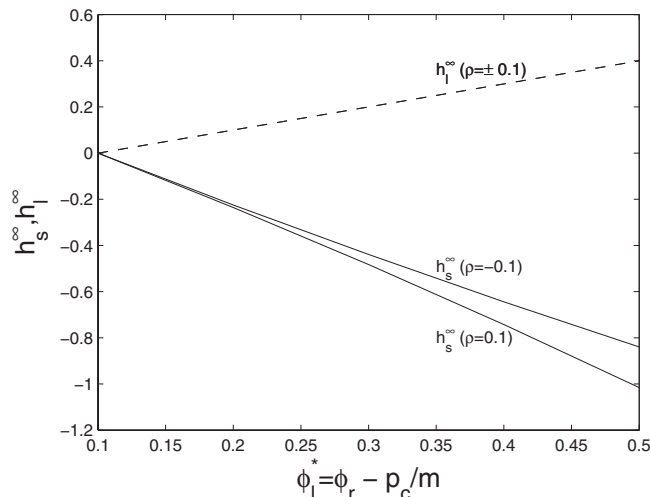


FIG. 4. This is a plot of \bar{h}_s^∞ and \bar{h}_ℓ^∞ as a function of ϕ_ℓ^* for $\phi_0=0.33$, $\phi_r=0.1$, and $\rho = \pm 0.1$.

times are also indicated along this curve, indicating agreement between numerical and analytical results. Three different one-dimensional deformable material figures are also shown in this plot to represent the dependence of deformation on ρ . In particular, we observe that solid deformation increases with increasing ρ .

In Fig. 4 we explore the dependence of the interface positions on the capillary pressure. First observe that when ϕ_ℓ^* is equal to ϕ_r (i.e., capillary pressure is zero), no fluid is imbibed by the porous material; here $\bar{h}_s^\infty, \bar{h}_\ell^\infty$ equal zero. As the capillary suction increases (i.e., ϕ_ℓ^* increases) the porous material starts deforming. This rate of deformation depends on the value of ρ . For $\rho=-0.1$, the deformation in the porous material is smaller compared to $\rho=0.1$. As mentioned in the discussion of Fig. 3, the height of fluid \bar{h}_ℓ^∞ depends linearly on ϕ_ℓ^* [see also Eq. (29)].

Figure 5 shows a plot of $\bar{h}_s^\infty, \bar{h}_\ell^\infty$ versus ϕ_r for different

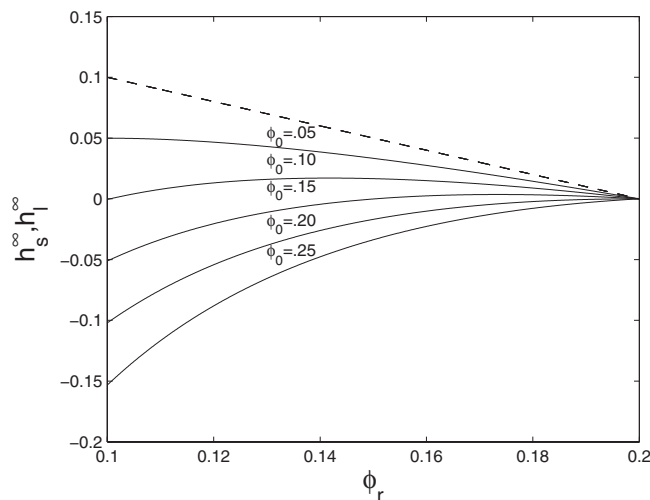


FIG. 5. This plot shows \bar{h}_s^∞ and \bar{h}_ℓ^∞ vs ϕ_r . The dashed line shows \bar{h}_ℓ^∞ and the solid lines show \bar{h}_s^∞ for different ϕ_0 values. We have used $\rho=0.1$ and $\phi_\ell^*=0.20$.

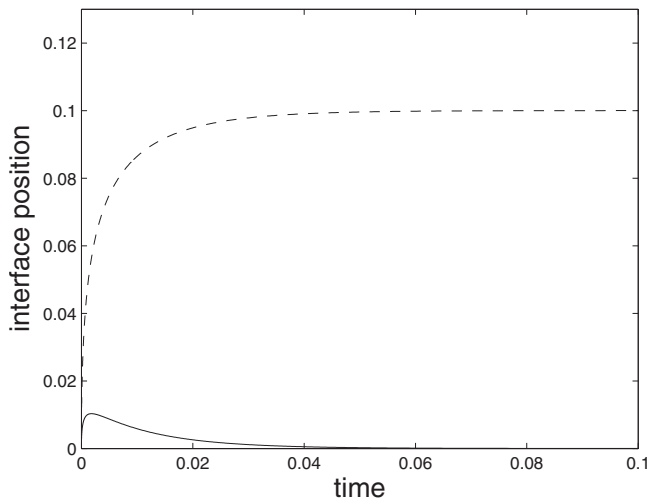


FIG. 6. This plot shows the interface positions (\bar{h}_ℓ , dashed line; \bar{h}_s , solid line) as a function of time for a special set of parameters that results in $\bar{h}_s^\infty = 0$. In particular, we have used $\rho=0.1$, $\phi_r=0.10$, $\phi_0=0.0995$, and $\phi_\ell^*=0.20$.

values of ϕ_0 . Note that \bar{h}_ℓ^∞ , indicated by the dashed line, is independent of ϕ_0 . Situations of net compression (\bar{h}_s^∞ positive) generally correspond to relatively small values of ϕ_0 . In order for this to be physically realistic, we assume that the liquid bath remains in contact with the solid even in cases with $\bar{h}_s > 0$. On the other hand, net expansion (\bar{h}_s^∞ negative) generally corresponds to relatively large values of ϕ_0 . For the intermediate values of ϕ_0 , details of other parameter values determine the nature of the final configuration. This suggests that materials with relatively high porosity tend to shrink while those with sufficiently low porosity tend to expand.

Figure 6 shows the interface positions (\bar{h}_s, \bar{h}_ℓ) as a function of time for a particular choice of parameter values for which $\bar{h}_s^\infty = 0$. Initially, the porous solid material shrinks, marked by positive h_s . Again, in order for $\bar{h}_s > 0$ to be physically realistic, we assume that the liquid bath remains in contact with the solid for all times. The overall behavior is that fluid rises to an equilibrium height and the wet solid interface rises initially but then returns to $\bar{z}=0$ (no net deformation). However, as we show in the next plot there is local compression (relative to ϕ_0) near the bottom of the wet material and local expansion (relative to ϕ_0) near the top of the wet material. The opposite trend to that shown in Fig. 6 can also be observed where initially the porous material expands ($h_s < 0$) before the solid interface position returns to $\bar{z}=0$.

Figure 7 shows a plot of solid volume fraction ϕ as a function of \bar{z} for both steady state and unsteady cases. Good agreement between the numerical and steady state solution is found. Both are compared with a constant solution ϕ_0 indicated by dashed line. In this plot we have used a special value of ϕ_0 such that $\bar{h}_s^\infty = 0$. When $\phi > \phi_0$ the solid material is in a state of relative compression. When $\phi < \phi_0$ the solid material is in a state of relative expansion. When $\rho > 0$, the local expansion ($\phi < \phi_0$) occurs near the top while the local compression ($\phi > \phi_0$) occurs near the bottom. Note in this

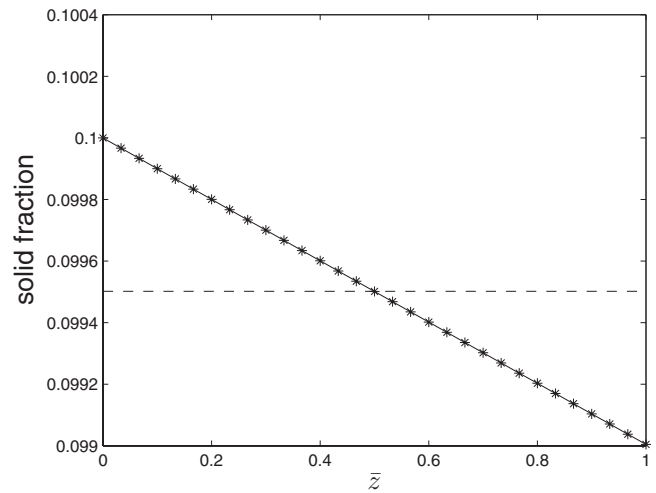


FIG. 7. This plot shows solid fraction vs \bar{z} for the long time state associated with the previous figure. The solid line denotes the unsteady $\phi(\bar{z}, \bar{t})$ for $t \rightarrow \infty$ and * denotes the steady ϕ solution. The dashed line denotes $\phi = \phi_0$ as reference. In these calculations, $\phi_0=0.0995$, $\phi_r=0.10$, $\phi_\ell^*=0.20$, and $\rho = 0.1$ which imply $\bar{h}_s^\infty = 0$.

case that there is local deformation as described but no net deformation (i.e., $h_s^\infty = 0$). This behavior is in fact true in general, as can be seen from a derivative of the equilibrium solid fraction,

$$\frac{d\phi}{d\bar{z}} = -\rho\phi_r(\bar{h}_\ell^\infty - \bar{h}_s^\infty)e^{\rho(\bar{h}_s^\infty - \bar{h}_\ell^\infty)\bar{z}}, \quad (40)$$

from Eq. (26). That is, when $\rho > 0$ the solid fraction decreases with increasing vertical position. The opposite trend occurs when $\rho < 0$; namely, the solid fraction increases with increasing vertical position. Finally, when $\rho = 0$ this equation shows that the equilibrium solid fraction is uniform throughout the solid, with value $\phi = \phi_r$. Physically, when $\rho_s > \rho_\ell$ the solid material tends to preferentially accumulate near the bottom and when $\rho_\ell > \rho_s$ liquid tends to preferentially accumulate near the bottom.

V. DRAINAGE INTO A DEFORMABLE POROUS MATERIAL

In the previous problem capillarity drove fluid flow in opposition to gravity. In this section we consider the opposite scenario in which capillary and gravitational forces act in the same direction. In this setting, at time $t=0$ we consider a finite amount of liquid with thickness H_0 in contact with the deformable porous material. The pressure at $z=H(t)$ is atmospheric pressure. The initial contact position of the liquid and porous material is defined by $z=0$. For time $t > 0$ the liquid starts penetrating into the porous material. The upper interface of the porous material after deformation is defined by $z=h_s(t)$ and the lower interface formed due to liquid penetration is defined by $z=h_\ell(t)$ as shown in Fig. 8.

The governing equations (1)–(4) are the same as before in the wet region. Similarly, after combining Eqs. (1), (7), and (8) we get the same PDE for ϕ [Eq. (9)] on $h_\ell(t) < z < h_s(t)$.

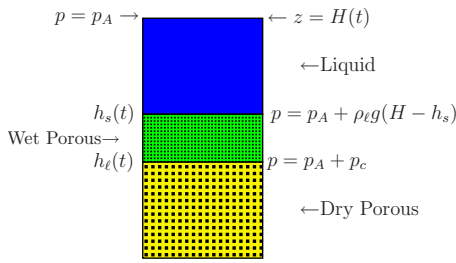


FIG. 8. (Color online) This figure shows the schematic of the one-dimensional liquid penetration configuration.

The boundary conditions applied at the liquid–wet material interface $z=h_s(t)$ are

$$w_s(h_s^-, t) = \frac{\partial h_s}{\partial t}, \quad (41)$$

$$p(h_s^-, t) = p_A - \rho_{\ell} g [h_s(t) - H(t)], \quad (42)$$

$$\sigma(h_s^-, t) = 0. \quad (43)$$

Here we have neglected inertial effects in the liquid region to get the hydrostatic pressure condition (42). The boundary conditions applied at the wet material–dry material interface $z=h_{\ell}(t)$ are

$$w_{\ell}(h_{\ell}^+, t) = \frac{\partial h_{\ell}}{\partial t}, \quad (44)$$

$$p(h_{\ell}^+, t) = p_A + p_c. \quad (45)$$

We introduce the same dimensionless quantities as before to nondimensionalize Eq. (9) on $h_{\ell}(t) < z < h_s(t)$ except that here we take

$$\bar{z} = \frac{z - h_{\ell}(t)}{h_s(t) - h_{\ell}(t)}. \quad (46)$$

The dimensionless PDE for ϕ can be written as

$$\begin{aligned} \frac{\partial \phi}{\partial \bar{t}} + \left[\frac{(\bar{z} - 1) \frac{d\bar{h}_{\ell}}{d\bar{t}}}{(\bar{h}_s - \bar{h}_{\ell})} - \frac{\bar{z}}{(\bar{h}_s - \bar{h}_{\ell})} \frac{d\bar{h}_s}{d\bar{t}} \right] \frac{\partial \phi}{\partial \bar{z}} + \frac{\bar{c}(\bar{t})}{(\bar{h}_s - \bar{h}_{\ell})} \frac{\partial \phi}{\partial \bar{z}} \\ = \frac{1}{(\bar{h}_s - \bar{h}_{\ell})^2} \frac{\partial^2 \phi}{\partial \bar{z}^2} + \frac{\rho}{(\bar{h}_s - \bar{h}_{\ell})} \frac{\partial \phi}{\partial \bar{z}}, \end{aligned} \quad (47)$$

where the function $\bar{c}(\bar{t})$ is given by

$$\bar{c}(\bar{t}) = \frac{1 - \phi_0}{\phi_0} \left[\frac{1}{(1 - \phi)(\bar{h}_s - \bar{h}_{\ell})} \frac{\partial \phi}{\partial \bar{z}} + \frac{\rho \phi}{(1 - \phi)} \right] \Bigg|_{\bar{z}=0}. \quad (48)$$

The PDE (47) is subject to the boundary conditions

$$\phi = \phi_r \quad \text{at} \quad \bar{z} = 1, \quad (49)$$

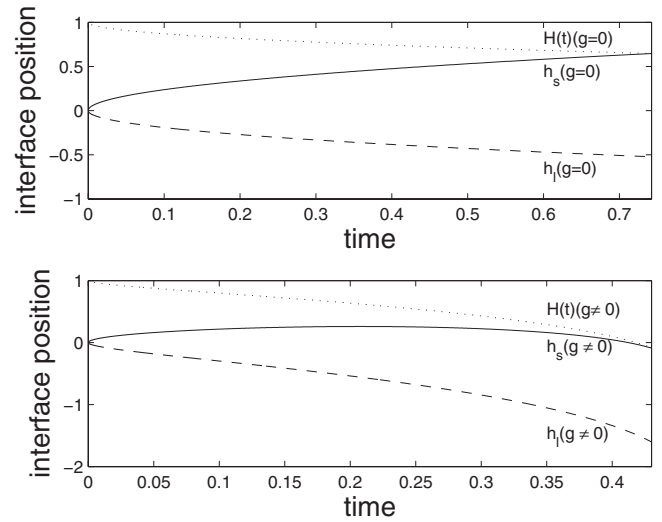


FIG. 9. This plot shows the evolution of the interface positions \bar{h}_s , \bar{h}_{ℓ} and $\bar{H}(t)$ for $g=0$ and $g \neq 0$ when a finite amount of liquid penetrates into the deformable porous material. In this plot we have used $\phi_{\ell}^* = 0.2$, $\phi_r = 0.1$, $\phi_0 = 0.33$, and $\rho = 0.1$.

$$\phi = \phi_{\ell}^* + \bar{H} - \bar{h}_s + (\bar{h}_s - \bar{h}_{\ell}) \int_0^1 (\rho \phi + 1) d\bar{z} \quad \text{at} \quad \bar{z} = 0. \quad (50)$$

Note that if $g=0$, condition (50) reduces to $\phi = \phi_{\ell}^*$. The boundary condition (50) is obtained by integrating Eq. (8) and applying the pressure boundary conditions (42) and (45). The liquid height $\bar{H}(t)$ follows from conservation of liquid,

$$\bar{H}(t) = \bar{H}_0 + \bar{h}_s - (\bar{h}_s - \bar{h}_{\ell}) \int_0^1 (1 - \phi) d\bar{z}, \quad (51)$$

where \bar{H}_0 is the dimensionless initial height of the liquid region.

The dimensionless interface positions satisfy the ODEs

$$\frac{d\bar{h}_s}{d\bar{t}} = \bar{c}(\bar{t}) - \left[\frac{1}{\phi(\bar{h}_s - \bar{h}_{\ell})} \frac{\partial \phi}{\partial \bar{z}} + \rho \right] \Bigg|_{\bar{z}=1}, \quad (52)$$

$$\frac{d\bar{h}_{\ell}}{d\bar{t}} = \bar{c}(\bar{t}) + \left[\frac{1}{(1 - \phi)(\bar{h}_s - \bar{h}_{\ell})} \frac{\partial \phi}{\partial \bar{z}} + \frac{\rho \phi}{(1 - \phi)} \right] \Bigg|_{\bar{z}=0}. \quad (53)$$

The initial conditions for the interface positions are

$$\bar{h}_{\ell}(\bar{t}=0) = 0, \quad \bar{h}_s(\bar{t}=0) = 0, \quad \text{and} \quad \bar{H}(\bar{t}=0) = \bar{H}_0. \quad (54)$$

We will use the same solution technique as before to solve Eqs. (47)–(54).

Figure 9 shows interface positions \bar{h}_s , \bar{h}_{ℓ} , and \bar{H} as a function of time. A finite amount of liquid is supplied whose thickness is shown by $\bar{H}(t)$ in the plot. Note that in the absence of gravity, the solution does not depend on ρ . Here, both curves $\bar{h}_s(t)$ and $\bar{h}_{\ell}(t)$ follow the similarity solution of the case of the zero gravity capillary rise problem until the

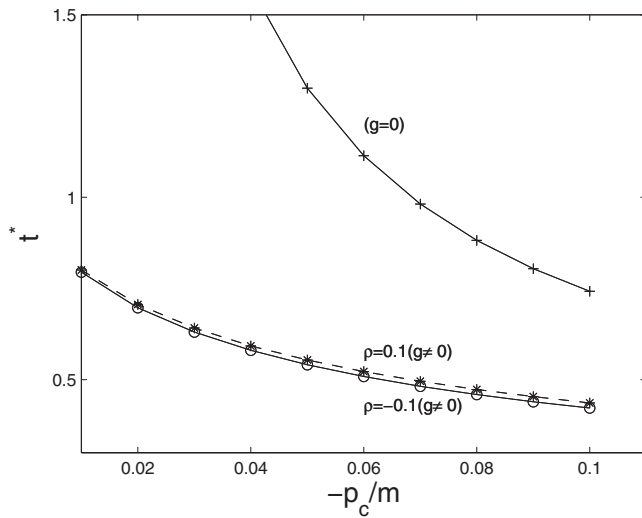


FIG. 10. This is a plot of drainage time (t^*) vs dimensionless capillary pressure. We have used $\phi_r=0.1$ and $\phi_0=0.33$. The upper curve shown by + is for the zero gravity case; here note that the $g=0$ solution does not depend on ρ . For nonzero gravity, the curve with * is for $\rho=0.1$ and the curve with \circ is for $\rho=-0.1$.

fluid layer is completely drained into the porous material when $\bar{h}_s=\bar{H}$. For the nonzero gravity case, both curves follow the similarity solution initially but then depart from this trend until again the liquid layer has completely drained. We define a drainage time as the time at which all the liquid is drained into the porous material $\bar{t}=t^*$ [$\bar{h}_s(t^*)=\bar{H}(t^*)$]. This drainage time is faster for the nonzero gravity case as compared to the zero gravity case.

Figure 10 shows the drainage time (t^*) as a function of dimensionless capillary pressure $-p_c/m$. As capillary suction is increased the drainage time t^* decreases. When gravity is present, this quantity depends on the density ratio ρ . In particular, the drainage time is larger when $\rho>0$ (solid more dense than liquid) as compared to when $\rho<0$ (solid less dense than liquid). In the absence of gravity increasing the capillary suction also decreases t^* . For the zero gravity case, the drainage time is independent of ρ .

VI. CONCLUSION

We have considered a one-dimensional model of capillary flow into a deformable porous material in the presence of gravity. This model is based on the work of Barry and Aldis,²⁵ Preziosi *et al.*,¹² and Anderson³⁴ and is similar to other models of flow in deformable materials.^{11,35,36} Our new contribution is a set of analytical and numerical results that detail the effects of gravity and capillarity on the material deformation in these systems. Our capillary-rise results of deformable porous materials are analogous to the classical Washburn results for capillary rise in rigid porous materials.

In the presence of gravity initially both interface positions, separating the liquid bath and wet porous material and dry porous material and wet porous material, follow the square root in time behavior as in the zero gravity case. However, in contrast to the zero gravity case where no steady state exists, the interface positions ultimately reach steady

state values \bar{h}_s^∞ and \bar{h}_ℓ^∞ . This fluid motion and solid deformation is driven by capillary suction; when capillary pressure is zero no fluid is imbibed into the material and consequently no deformation occurs.

We have quantified the deformation and imbibition dependence on fundamental quantities such as the strength of capillary suction and the solid-liquid density ratio. Deformation on both local and global scales has been assessed. Increased capillary pressure leads to increased net deformation. Also the net deformation of the solid increases with increasing $\rho=(\rho_s/\rho_\ell-1)$. The deformation within the sponge has also been assessed. In particular, when the solid is more dense than the liquid we observe that there is local expansion near the top and local compression near the bottom. An opposite trend is observed when the solid is less dense than the liquid; here there is local expansion near the bottom and local compression near the top.

In our capillary rise configuration, the equilibrium rise height of liquid is the same for both rigid and deformable geometries assuming the same capillary pressure in both cases. This is also related to our assumption that the pressure is fixed at a fixed location $\bar{z}=0$ rather than at the bottom of deforming solid. Therefore the noted increase in net deformation is measured by the position of the wet sponge-liquid interface.

We have also examined the case in which capillary and gravitational forces act in the same direction. Here we measure the time required for a finite volume of fluid to penetrate into the deformable material. It is observed that drainage of liquid is faster for the nonzero gravity case as opposed to when gravity is absent. We have also observed that drainage time decreases as capillary suction is increased. When gravity is present we find that when the solid is more dense than the liquid, the drainage time is slower than when the solid is less dense than the liquid.

As we show in the Appendix, the early time dynamics observed in the experiments are consistent with the early time $t^{1/2}$ dynamics predicted by the theory for capillary rise and material deformation. As was the case for capillary rise in rigid porous materials (e.g., Refs. 3 and 4) we find that the experimental data do not conform to the late time equilibrium predictions of our theory. The complete understanding of these differences is only beginning to be addressed for rigid porous materials and so we hope that information gained in that context will lead to new ideas for deformable materials.

These capillary and gravity interactions in one-dimensional deformable porous materials highlight a number of interesting phenomena that suggest further analysis of models in higher dimensions as well as further experiments.

ACKNOWLEDGMENTS

The authors would like to acknowledge support from the U.S. National Science Foundation, NSF Award No. DMS-0709095. The authors would also like to thank Robert Allen, G. B. McFadden, and K. J. Wahl for helpful discussions.

APPENDIX: EXPERIMENTS ON CAPILLARY RISE OF A LIQUID INTO A DEFORMABLE SPONGE

We present experimental results that document both the capillary rise of water into an initially dry sponge and the resulting deformation of the sponge. We discuss these results in the context of capillary rise experiments that have previously been performed for rigid porous materials as well as in the context of the theoretical model presented in the main text.

The classical model of Washburn¹ has been used for nearly a century to describe capillary flow in rigid porous materials. Washburn's model predicts that when a fluid is imbibed into a porous material due to capillarity and against the force of gravity the fluid height initially increases, following a square root in time behavior before approaching an equilibrium value determined by the balance of capillary forces with the weight of the elevated fluid.

Recent experimental work on capillary rise in rigid porous materials has verified Washburn's early time $t^{1/2}$ power law but has also shown that at later times, rather than reaching an equilibrium height, the fluid may continue to rise following a different power law. Delker *et al.*³ conducted experiments on capillary rise of water in a porous material made up of glass beads. In this setting they observed the early time $t^{1/2}$ power law predicted by Washburn but demonstrated that even after several orders of magnitude in time beyond the early scaling regime, the fluid height continued to increase, following dynamics that could be fitted with a power law $t^{1/4}$. They attributed these long time dynamics to randomness in the capillary forces of the porous material. More recently, Lago and Araujo⁴ conducted similar experiments for capillary rise of water in a packing of glass beads as well as capillary rise of water in Berea sandstones. For their experiments with glass beads they, like Delker *et al.*, observed the early time Washburn dynamics and long time dynamics for height that followed a power law (they did not give a specific value for this power law, but it appears to be close to the $t^{1/4}$ estimated by Delker *et al.*). In contrast, for the case of Berea sandstone only the $t^{1/2}$ power law was observed.

In our experiments on capillary rise of water in deformable sponges presented below, we measure the capillary rise height $h_l(t)$ relative to the water level $z=0$ of the fluid bath, the sponge deformation depth $h_s(t)$ into the bath, and the overall wet sponge height $h(t)=h_l(t)-h_s(t)$. We observe behavior analogous to that observed by Delker *et al.*³ and Lago and Araujo⁴ for their experiments with glass beads and water. Namely, we observe that the capillary rise height $h_l(t)$ and deformation depth $h_s(t)$ follow early time dynamics consistent with a $t^{1/2}$ power law. The long time dynamics that we observe in the experiments for $h_l(t)$ can be characterized by a power law t^b with $0.22 < b < 0.25$, which appears to be close to the $t^{1/4}$ observed in rigid porous materials. The power law observed for $h_s(t)$ has a slightly smaller exponent ranging from 0.18 to 0.21.

1. Description of experiments

In our experiments we use commonly available cellulose sponges (e.g., kitchen sponges) and water. Four sponges, all cut from a single larger sponge, were used in the experiments described here. The four smaller sponges were approximately rectangular parallelepipeds and when damp had height of 9.1 ± 0.1 cm, width of 3.8 ± 0.2 cm, and depth of 2.4 ± 0.1 cm. These same sponges when dry (as at the beginning of each experiment) had height of 8.1 ± 0.2 cm, width of 3.5 ± 0.2 cm, and depth of 2.1 ± 0.1 cm. The variations listed are representative of the variation of each dimension within a given sponge as well as that between the individual sponges. In general it is difficult to avoid such variations in at least either the wet and dry sponges. While careful milling or cutting of a sponge can be done (e.g., Ref. 11) the sponge deforms during both wetting and drying and in general will not exactly maintain its shape. We note that while it is possible to compress a sponge as it dries, for example, for more efficient storage and transport of dry sponges as well as more dramatic deformation when it soaks up liquid, in all the cases presented, the sponges were allowed to dry naturally (without external compression) and completely before each experiment. Further, we did not attempt to eliminate changes in the sponge properties that may have occurred over multiple wetting, drying, swelling, and shrinking cycles as has been reported in other similar experiments for polyurethane sponges (see Refs. 39–41 and 11). While presumably the material properties may vary between experiments conducted here, our interest is primarily in identifying qualitative behavior of typical sponges (e.g., ones that may not have undergone multiple compression cycles to equilibrate material properties) and to document joint capillary rise and material deformation in an experimental setting. Our results show no qualitative changes in the imbibition/deformation process during the course of experiments run on the same sponges over several months.

A typical experiment was conducted as follows. A clear-sided tank with inside height of 14 cm, width of 26.1 cm, and length of 20.3 cm was partially filled with water. One of the sponges was then positioned along the front side of the tank so that the bottom of the sponge was still slightly above the water level. This sponge was securely attached with a clamp at the top of the tank but otherwise could deform freely. To begin each experiment, the water level was slowly raised by adding more water to the tank via a tube near the back and bottom of the tank. This filling was stopped as soon as the water level reached the bottom of the sponge and imbibition began. We observed no significant influence of the wall of the tank on the capillary rise in the sponge and resultant sponge deformation; the wet/dry sponge interface and the wet sponge/liquid interface were generally planar and parallel to the water level in the tank throughout the course of each experiment. A typical configuration is shown in Fig. 11 at a point in time after the imbibition/sponge deformation process had begun. The ruler on the right, which was taped to the inside of the tank, shows centimeter markings. A stop watch, not shown in this figure, was used to record the time. The duration of each experiment was approximately 35–40

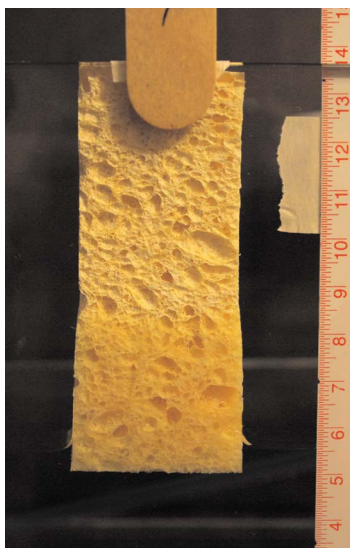


FIG. 11. (Color online) Fluid-induced deformation in a sponge: Water soaks into an initially dry sponge and leads to an approximately one-dimensional deformation of the sponge. The scale on the right shows centimeter markings. In this snapshot, the bottom of the sponge, $z=h_s(t)$, is at approximately the 5.0 cm mark, the water level, $z=0$, is at approximately 5.5 cm, and the interface between the wet and dry portions of the sponge, $z=h_l(t)$, is at approximately 8.5 cm.

min; this was the approximate amount of time required for the imbibed liquid to reach the upper clamped portion of the sponge. Photographs of the sponge, ruler, water level, and stopwatch were taken during the course of each experiment. Initially, the capillary rise and deformation occur rapidly and photographs were taken at approximately 3 frames/s for the first several seconds. As the dynamics slowed, the interval between photographs was increased up to a maximum of about 1 min for the last 15–20 min of the evolution. This process was repeated for several different sponges on several different days. Sponges were reused after they were allowed to dry completely.

Measurements were obtained from digitized photographs using software IMAGEJ (freeware for image analysis available from NIH) to record for each image positions of the wet sponge/dry sponge interface ($z=h_l$), the wet sponge/water interface ($z=h_s$), the water level ($z=0$), and markings on the ruler. The time for each image was also recorded. The software allowed us to record pixel values at a given location and a corresponding scale factor for conversion of pixels to centimeters was obtained by recording pixel values on the image of the ruler. Three points were identified along each interface h_s and h_l and then averaged to obtain a single value h (total distance between the averaged points for the upper and lower interface positions) representing the total thickness of the wet sponge region for each image. Numerical values for h_s and h_l were obtained from the averaged positions recorded for each interface by computing their distance from the line representing the water level at $z=0$. An assumption made in the analysis was that there was negligible change in the water level of the bath during the course of each experiment. Based on the quantity of water taken up by the sponge and on the tank dimensions we estimate that the change in

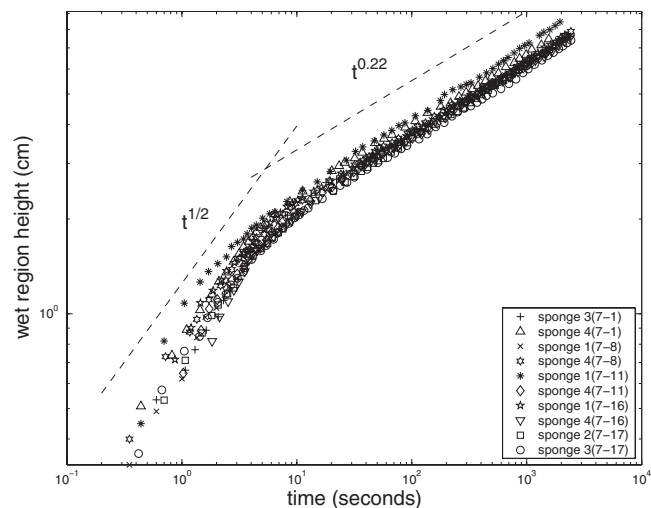


FIG. 12. This figure shows the measured values of $h=h_l-h_s$ as a function of time for the ten different experiments. Also shown as a guide are two thin dashed lines above the data indicating a $t^{1/2}$ power law at early times and a $t^{0.22}$ power law at later times.

water level was less than 0.5 mm during the course of each experiment. If one also accounts for the volume of deformed solid below the water line the estimated change in water level would be even smaller. Care was taken to avoid any motion of the tank or camera during each experiment. Preliminary experiments in which the sponge was lowered into the water resulted in slight motion of the sponge during initial stages of imbibition and have not been included in the data presented here. However, in those cases, the value of h could be measured robustly even when the values of h_s and h_l revealed where sponge motion occurred. That is, the measured value of h is essentially independent of the recorded water level, unlike h_s and h_l which are determined relative to the recorded water level.

Figures 12–14 show the experimental results and some comparisons to the theory that are described in more detail below. Figure 12 shows the recorded value of the overall wet sponge height h as a function of time for ten different experiments. Figures 13 and 14 show similar results for the wet/dry sponge interface h_l and the wet sponge/water interface h_s . We point out here that since h_s is negative we have actually plotted $|h_s|$ in order to make use of log-log scales. Two important trends can be observed from these figures. First, there is an initial regime in which both interface positions h_l and h_s follow a power law in time that is consistent with the $t^{1/2}$ power law predicted by the model. This time regime corresponds to approximately the first 8 or 9 s of the experiment. We refer to this as the early time scaling regime. For longer times, there is a transition to a second power law that is slower; dashed lines show a power law $t^{0.22}$ in Figs. 12 and 13 for h and h_l and a power law $t^{0.2}$ in Fig. 14 for h_s . We refer to this as the later time scaling regime.

As noted above, the experimental data for h , h_s , and h_l were fitted to power laws

$$h = qt^p, \quad |h_s| = q_s t^{p_s}, \quad h_l = q_l t^{p_l}, \quad (\text{A1})$$

where t is the elapsed time from the beginning of imbibition for both early time and later time regimes. The values for p ,

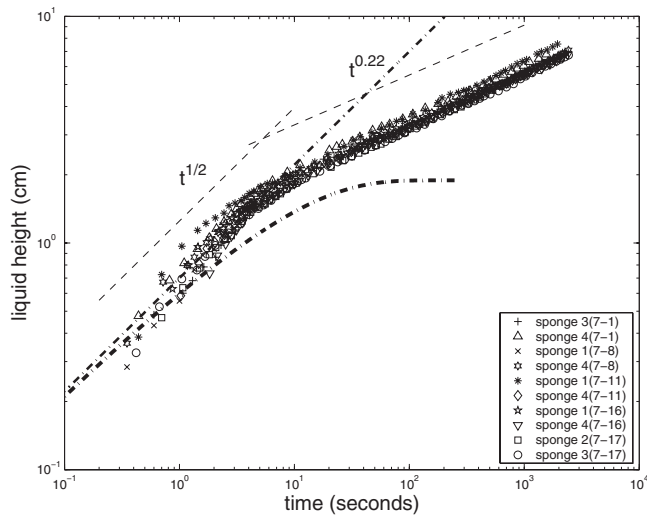


FIG. 13. This figure shows the measured values of h_l as a function of time for the ten different experiments. Also shown as a guide are two thin dashed lines above the data indicating a $t^{1/2}$ power law at early times and a $t^{0.22}$ power law at later times. Additionally, we have included dashed-dotted curves that show predictions from the theory without gravity (thinner dashed-dotted line) and with gravity (thicker dashed-dotted curve).

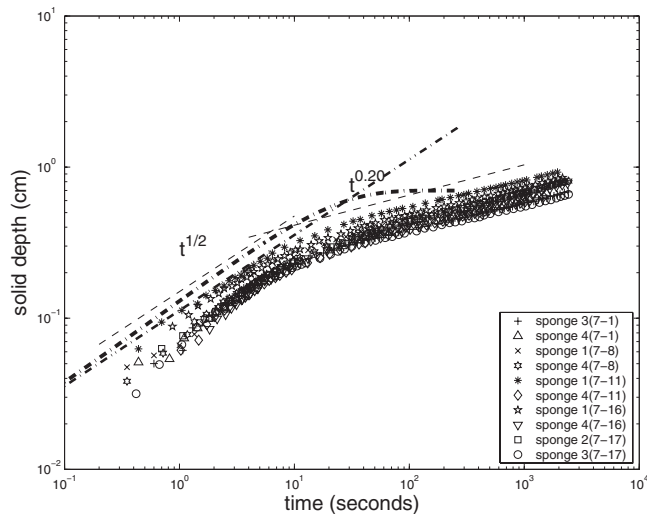


FIG. 14. This figure shows the measured values of $|h_s|$ as a function of time for the ten different experiments. Also shown as a guide are two thin dashed lines above the data indicating a $t^{1/2}$ power law at early times and a $t^{0.20}$ power law at later times. Additionally, we have included dashed-dotted curves that show predictions from the theory without gravity (thinner dashed-dotted line) and with gravity (thicker dashed-dotted curve).

q , p_s , q_s , p_l , and q_l are listed for each experiment in Tables I and II. For the early time regime we find exponents between 0.47 and 0.56 for h , 0.47–0.59 for h_s , and 0.47–0.57 for h_l . For the later time regime we find exponents between 0.22 and 0.24 for h , 0.18 and 0.21 for h_s and 0.22 and 0.25 for h_l . We note that these values are sensitive to the precise value identified as the starting time. Our experimental data for the early times included photographs taken at a rate of 3 frames/s which allowed us to visually identify the starting time to within approximately 0.1–0.2 s. The scatter in the data is representative of the sensitivity of the parameter fits to the uncertainty in the starting time. The power law for h_l in the late time regime is close to the $t^{1/4}$ observed by Delker *et al.*³ and Lago and Araujo⁴ for capillary rise of water in glass beads. The later time power law observed here for deformation h_s is also close to this value but appears to be slightly smaller. That the late time power law exponent for h is much closer to h_l than h_s is consistent with the fact that h_l is roughly ten times larger than $|h_s|$ and so a fit of $h = h_l - h_s$ would be dominated by the behavior of h_l . As a check of our data processing we have confirmed that the value of h computed from the pixel data and the values of h_l and h_s computed from the pixel data are consistent in that $h_l - h_s$ is within 10^{-14} of h (in cm).

2. Comparison to theory

Our first and primary point of comparison between the theory and the experiment is in the early time power law scaling with respect to time. The theoretical prediction for the capillary rise and sponge deformation can be expressed most clearly in terms of the zero gravity similarity solution for the interface positions given by

$$h_l(t) = 2\lambda_l \sqrt{Dt}, \quad (\text{A2})$$

$$h_s(t) = 2\lambda_s \sqrt{Dt}. \quad (\text{A3})$$

The coefficients λ_l and λ_s are constants determined by parameters ϕ_l^* , ϕ_0 , and ϕ_r (e.g., see main text or Ref. 34 for details). The values of h_l and h_s also depend on $D = K_0 m / \mu$, where K_0 is a reference permeability, m is a stress scale, and μ is the fluid viscosity. The experimentally measured power law fits for the wet sponge/dry sponge interface h_l and the wet sponge/liquid interface h_s , shown in Table I, are consis-

TABLE I. Early time scaling fits from the experiments based on approximately the first 8–9 s of evolution.

Sponge (date)	p	q	p_s	q_s	p_l	q_l
3 (7-1)	0.55	0.68	0.59	0.071	0.55	0.61
4 (7-1)	0.51	0.84	0.55	0.072	0.50	0.77
1 (7-8)	0.56	0.67	0.55	0.073	0.57	0.60
4 (7-8)	0.50	0.80	0.56	0.074	0.49	0.73
1 (7-11)	0.49	0.94	0.50	0.11	0.49	0.83
4 (7-11)	0.50	0.74	0.56	0.065	0.50	0.68
1 (7-16)	0.47	0.86	0.47	0.10	0.47	0.76
4 (7-16)	0.52	0.68	0.57	0.064	0.52	0.62
2 (7-17)	0.51	0.70	0.52	0.075	0.51	0.63
3 (7-17)	0.52	0.70	0.59	0.066	0.51	0.63

TABLE II. Late time scaling fits from experiments.

Sponge (date)	p	q	p_s	q_s	p_l	q_l
3 (7-1)	0.22	1.34	0.18	0.17	0.23	1.17
4 (7-1)	0.22	1.48	0.21	0.13	0.22	1.35
1 (7-8)	0.23	1.29	0.20	0.18	0.23	1.11
4 (7-8)	0.22	1.38	0.20	0.17	0.22	1.21
1 (7-11)	0.24	1.38	0.18	0.24	0.25	1.16
4 (7-11)	0.23	1.30	0.20	0.15	0.23	1.14
1 (7-16)	0.23	1.33	0.19	0.19	0.23	1.14
4 (7-16)	0.23	1.30	0.20	0.16	0.23	1.14
2 (7-17)	0.24	1.20	0.20	0.17	0.24	1.03
3 (7-17)	0.23	1.22	0.19	0.15	0.23	1.07

tent with the theoretical prediction of $1/2$. This provides support that the most basic capillary rise and deformation mechanisms observed experimentally are captured by the theory.

In order to obtain further comparison between the early time predictions of the theory and experiment we need to determine appropriate values for λ_l , λ_s (which require knowing ϕ_r , ϕ_0 , and ϕ_l^*), and D appearing in Eqs. (A2) and (A3).

We first obtain an estimate for ϕ_r , which is the ratio of the solid volume of the wet sponge to the total volume occupied by the wet sponge in its relaxed state. We take the total volume of the wet sponge (parallelepiped) to be $9.1 \times 3.8 \times 2.4 = 83.0 \text{ cm}^3$. We measured the solid volume of the wet sponge by submerging the sponge into a straight-sided container of water and compressing the sponge to remove all the trapped air. After the sponge was allowed to deform back to its relaxed state and while still submerged, we measured the change in the height of the water in the container. In this way we estimated the solid volume of the sponge to be 6.1 cm^3 . The ratio of these gives the estimate $\phi_r = 0.073$.

We interpret ϕ_0 as the ratio of the solid volume of the dry sponge to the total volume occupied by the dry sponge. In order to obtain an estimate for ϕ_0 for a typical sponge we make the assumption that the solid volume of the dry sponge is equal to the solid volume of the wet sponge. This implies that ϕ_0/ϕ_r is the ratio of the wet sponge volume to dry sponge volume, which is $(9.1 \times 3.8 \times 2.4)/(8.1 \times 3.5 \times 2.1) = 1.39$. This leads to the estimate $\phi_0 = 0.10$.

The theory also involves the parameter ϕ_l^* which represents the solid fraction in the wet sponge at the wet sponge-dry sponge interface. For simplicity and lack of a direct measurement of this quantity we shall assume that $\phi_l^* = \phi_0$. That is, there is no jump in the solid volume fraction at the wet/dry sponge interface. With $\phi_l^* = \phi_0 = 0.10$ and $\phi_r = 0.073$, the values for the coefficients in Eqs. (A2) and (A3) computed from the model are $\lambda_l = 0.3675$ and $\lambda_s = -0.0590$.

In principle the value of D could be obtained from measurements of the parameters K_0 and m representing reference values for permeability and stress. However, the models for permeability and stress used in the model from which these two parameters originate were chosen based on expected qualitative behavior and so presumably measurements of the full stress and permeability dependence on the solid fraction

ϕ would be required for a completely qualitative comparison. While such measurements have been obtained for other sponges (e.g., see Ref. 11) we do not attempt such measurements here. Instead, we shall obtain D by relating it to the fitting value of q_l from the experimental data. In particular, we determine its value by comparison of Eq. (A2) to the obtained values of q_l (see Table I) and the above computed values of λ_l by

$$D = \frac{q_l^2}{4\lambda_l^2}. \quad (\text{A4})$$

In the results shown we have chosen $q_l = 0.7$ as a representative value of those listed in Table I.

The predictions for the zero gravity $h_l(t)$ and $h_s(t)$ given in Eqs. (A2) and (A3) based on the value $q = 0.7$ are shown in Figs. 13 and 14 as the thinner dashed-dotted lines. These lines have a slope of $1/2$. While these predictions do not perfectly fit the collection of curves shown, we note that only one parameter value was fitted, namely, D , in order to obtain this comparison. In fact, the difference between the thin dashed-dotted line and the early time data in Fig. 14 for $|h_s|$ is a reasonable estimate of the agreement between theory and experiment since once D was chosen to fit the h_l data, there were no further adjustable parameters for h_s . Improved comparison between the theoretical curve and the experimental data could be obtained at the expense of fitting an additional parameter. For example, we have observed from the experimental data that the ratio h_l/h_s is approximately -10 . In the theory this translates to the ratio of $\lambda_l/\lambda_s = -10$ and so this requirement could be imposed on the theory to suggest an alternate choice for a parameter such as ϕ_r , ϕ_0 , or ϕ_l^* . We have chosen not to do so in favor of fitting the fewest number of parameters as possible.

As pointed out earlier, the experimental data for later times do not show that equilibrium is reached but rather indicate that the evolution continues following another power law. The theory described in the main text, as was the case for the classical Washburn equation for rigid porous materials, does not predict these long time dynamics. Despite this, for completeness we include two additional curves that show the results of the full model prediction with gravity. In Figs. 13 and 14 these appear as the thicker dashed-dotted

curves. In order to plot the full results with gravity, the values of two additional parameters are required. The first is the length scale $L=m/(\rho_l g)$ and the second is the density ratio parameter $\rho=\rho_s/\rho_l-1$. Since the length scale L depends on the parameter m (recall D depended on both K_0 and m) we again take the approach of not attempting to measure this parameter directly. Rather, we have selected a value of L so that the predicted equilibrium height for h_l falls near its representative early time/late time transition region in the experimental data. In the experiments of Lago and Araujo⁴ the Washburn equilibrium height occurred at a similar location with respect to the experimental data. We have used $L=70$ cm which, with $\rho_l=10^3$ kg m⁻³ and $g\approx 10$ m s⁻² implies that $m=7\times 10^3$ Pa. Lastly, while we have not measured ρ directly, we have observed experimentally that the sponge is more dense than the water so that $\rho>0$. However, the theoretical predictions with different values of ρ reveal no significant change in the positions of the thick dashed-dotted curves in Figs. 13 and 14 and so the calculations we have shown have used $\rho=0$ for simplicity. The resulting theoretical values for $|h_s|$ overpredicts the experimental data. However, again we emphasize that only one additional parameter, L , was fitted and so no parameters were adjusted specifically for the h_s comparison.

Some differences between the theory and experiments even for the early time regime may be attributable to complexities in the experiments that are not accounted for in the model. For example, it is worth pointing out that the quantity of fluid taken up by the sponge is actually much less than the available pore space in the sponge. One estimate for the liquid fraction in the wet sponge based on solid fraction alone would be $1-\phi_r\approx 0.93$. However, based on more direct measurements this appears to be too high. Our directly measured estimate for the volume of liquid taken up by the sponge after an experiment is 17.5 ± 1 cm³ which corresponds to a liquid fraction of around 0.2. This total amount of liquid, estimated for different experiments by measuring the volume of water that could be squeezed out of the sponge immediately after the experiment was over, includes the liquid occupying the region of the wet sponge below the water level as well as above it. Based on this and the observation that a considerable amount of the pore space in the wet sponge was occupied by air, it seems safe to assume that the actual liquid fraction in the wet sponge is considerably less than the available pore space. The presence of a third, vapor, phase was not accounted for in the theory and may be important for improved agreement.

Just as our experiments are not fully explained by the theoretical model in the main text, we note that the experimental work of Delker *et al.*³ and Lago and Araujo⁴ was not completely explained by the classical Washburn model. In the latter case, this discrepancy has recently motivated Lockington and Parlange⁴² to develop a new model that generalized the Washburn model. Their new model predicts that, as in the experimental data, the capillary-driven liquid in the porous material continues to rise following dynamics characterized by a parameter related to the presence of saturation gradients in the system. While the incorporation of the recent ideas of Lockington and Parlange have not been considered

in the present model for fluid flow and deformation, the development of more sophisticated models along these lines is an exciting avenue for future research.

3. Conclusions

In conclusion, we have presented experimental data that show capillary rise in a deformable porous sponge. Early time data were observed to follow approximately a $t^{1/2}$ power law and was found to be generally consistent with the theoretical predictions. The experimental data also revealed a long time regime, not predicted theoretically, in which both the fluid height and sponge deformation followed a power law that was clearly slower than the early time $t^{1/2}$ scaling; estimates suggest $t^{0.22}$ for the liquid height and $t^{0.2}$ for the solid deformation. These are comparable to the approximate $t^{1/4}$ power law for an analogous long time regime observed for rigid porous materials.^{3,4}

- ¹E. W. Washburn, "The dynamics of capillary flow," *Phys. Rev.* **17**, 273 (1921).
- ²B. V. Zhmud, F. Tiberg, and K. Hallstenson, "Dynamic of capillary rise," *J. Colloid Interface Sci.* **228**, 263 (2000).
- ³T. Delker, D. B. Pengra, and P. Wong, "Interface pinning and the dynamics of capillary rise in porous media," *Phys. Rev. Lett.* **76**, 2902 (1996).
- ⁴M. Lago and M. Araujo, "Capillary rise in porous media," *J. Colloid Interface Sci.* **234**, 35 (2001); "Capillary rise in porous media," *Physica A* **289** 1 (2001).
- ⁵S. H. Davis and L. M. Hocking, "Spreading and imbibition of viscous liquid on a porous base," *Phys. Fluids* **11**, 48 (1999).
- ⁶S. H. Davis and L. M. Hocking, "Spreading and imbibition of viscous liquid on a porous base. II," *Phys. Fluids* **12**, 1646 (2000).
- ⁷M. Spiegelman, "Flow in deformable porous media. Part 1. Simple analysis," *J. Fluid Mech.* **247**, 17 (1993).
- ⁸M. Kaczmarek and T. Hueckel, "Chemico-mechanical consolidation of clays: Analytical solutions for a linearized one-dimensional problem," *Transp. Porous Media* **32**, 49 (1998).
- ⁹M. Kaczmarek, "Chemically induced deformation of a porous layer coupled with advective-dispersive transport. Analytical solutions," *Int. J. Numer. Analyt. Meth. Geomech.* **25**, 757 (2001).
- ¹⁰G. P. Peters and D. W. Smith, "Solute transport through a deforming porous medium," *Int. J. Numer. Analyt. Meth. Geomech.* **26**, 683 (2002).
- ¹¹J. L. Sommer and A. Mortensen, "Forced unidirectional infiltration of deformable porous media," *J. Fluid Mech.* **311**, 193 (1996).
- ¹²L. Preziosi, D. D. Joseph, and G. S. Beavers, "Infiltration of initially dry, deformable porous media," *Int. J. Multiphase Flow* **22**, 1205 (1996).
- ¹³V. J. Michaud, J. L. Sommer, and A. Mortensen, "Infiltration of fibrous preforms by a pure metal: Part V. Influence of preform compressibility," *Metall. Mater. Trans. A* **30**, 471 (1999).
- ¹⁴D. Ambrosi and L. Preziosi, "Modeling injection molding processes with deformable porous preforms," *SIAM J. Appl. Math.* **61**, 22 (2000).
- ¹⁵L. Billi and A. Farina, "Unidirectional infiltration in deformable porous media: Mathematical modeling and self-similar solution," *Q. Appl. Math.* **58**, 85 (2000).
- ¹⁶J. Feng and S. Weinbaum, "Lubrication theory in highly compressible porous media: The mechanics of skiing, from red cells to humans," *J. Fluid Mech.* **422**, 281 (2000).
- ¹⁷K. S. A. Chen and L. E. Scriven, "Liquid penetration into a deformable porous substrate," *Tappi J.* **73**, 151 (1990).
- ¹⁸A. D. Fitt, P. D. Howell, J. R. King, C. P. Please, and D. W. Schwendeman, "Multiphase flow in a roll press nip," *Eur. J. Appl. Math.* **13**, 225 (2002).
- ¹⁹M. H. Holmes, "A nonlinear diffusion equation arising in the study of soft tissue," *Q. Appl. Math.* **41**, 209 (1983).
- ²⁰M. H. Holmes, "Comparison theorems and similarity solution approximations for a nonlinear diffusion equation arising in the study of soft tissue," *SIAM J. Appl. Math.* **44**, 545 (1984).

- ²¹M. H. Holmes, "A theoretical analysis for determining the nonlinear hydraulic permeability of a soft tissue from a permeation experiment," *Bull. Math. Biol.* **47**, 669 (1985).
- ²²M. H. Holmes, "Finite deformation of soft tissue: Analysis of a mixture model in uniaxial compression," *J. Biomech. Eng.* **108**, 372 (1986).
- ²³M. H. Holmes and V. C. Mow, "The nonlinear characteristic of soft gels and hydrated connective tissue in ultrafiltration," *J. Biomech.* **23**, 1145 (1990).
- ²⁴J. S. Hou, M. H. Holmes, W. M. Lai, and V. C. Mow, "Boundary conditions at the cartilage-synovial fluid interface for joint lubrication and theoretical verifications," *J. Biomech. Eng.* **111**, 78 (1989).
- ²⁵S. I. Barry and G. K. Aldis, "Radial flow through deformable porous shells," *J. Aust. Math. Soc. Ser. B, Appl. Math.* **34**, 333 (1993).
- ²⁶S. I. Barry and G. K. Aldis, "Flow induced deformation from pressurized cavities in absorbing porous tissues," *Bull. Math. Biol.* **54**, 977 (1992).
- ²⁷S. I. Barry, K. H. Parker, and G. K. Aldis, "Fluid flow over a thin deformable porous layer," *J. Appl. Math. Phys. (ZAMP)* **42**, 633 (1991).
- ²⁸M. A. Biot, "General theory of three dimensional consolidation," *J. Appl. Phys.* **12**, 155 (1941).
- ²⁹M. A. Biot, "Consolidation settlement under a rectangular load distribution," *J. Appl. Phys.* **12**, 426 (1941).
- ³⁰M. A. Biot and F. M. Clingan, "Consolidation settlement of a soil with an impervious top surface," *J. Appl. Phys.* **12**, 578 (1941).
- ³¹M. R. Bowen, "Incompressible porous media models by use of the theory of mixtures," *Int. J. Eng. Sci.* **18**, 1129 (1980).
- ³²R. J. Atkin and R. E. Crain, "Continuum theories of mixture: Basic theory and historical development," *Q. J. Mech. Appl. Math.* **29**, 209 (1976).
- ³³W. Wang and K. H. Parker, "The effect of deformable porous surface layers on the motion of a sphere in a narrow cylindrical tube," *J. Fluid Mech.* **283**, 287 (1995).
- ³⁴D. M. Anderson, "Imbibition of a liquid droplet on a deformable porous substrate," *Phys. Fluids* **17**, 087104 (2005).
- ³⁵S. Manley, J. M. Skotheim, L. Mahadevan, and D. A. Weitz, "Gravitational collapse of colloidal gels," *Phys. Rev. Lett.* **94**, 218302 (2005).
- ³⁶C. Kim, Y. Liu, A. Kühnle, S. Hess, S. Viereck, T. Danner, L. Mahadevan, and D. A. Weitz, "Gravitational stability of suspensions of attractive colloidal particles," *Phys. Rev. Lett.* **99**, 028303 (2007).
- ³⁷E. R. Dufresne, E. I. Corwin, N. A. Greenblatt, J. Ashmore, D. Y. Wang, A. D. Dinsmore, J. X. Cheng, X. S. Xie, J. W. Hutchinson, and D. A. Weitz, "Flow and fracture in drying nanoparticle suspensions," *Phys. Rev. Lett.* **91**, 224501 (2003).
- ³⁸E. R. Dufresne, D. J. Stark, N. A. Greenblatt, J. X. Cheng, J. W. Hutchinson, L. Mahadevan, and D. A. Weitz, "Dynamics of fracture in drying suspensions," *Langmuir* **22**, 7144 (2006).
- ³⁹G. S. Beavers, K. Wittenberg, and E. M. Sparrow, "Fluid flow through a class of highly-deformable porous media. Part II. Experiments with water," *J. Fluids Eng.* **103**, 440 (1981).
- ⁴⁰K. H. Parker, R. V. Mehta, and C. G. Caro, "Steady flow in porous, elastically deformable materials," *J. Appl. Mech.* **54**, 794 (1987).
- ⁴¹Y. Lanir, S. Sauob, and P. Maresky, "Nonlinear finite deformation response of open cell polyurethane sponge to fluid filtration," *J. Appl. Mech.* **57**, 449 (1990).
- ⁴²D. A. Lockington and J.-Y. Parlange, "A new equation for macroscopic description of capillary rise in porous media," *J. Colloid Interface Sci.* **278**, 404 (2004).